

## RESEARCH ARTICLE

10.1002/2014JB011156

## Key Points:

- InSAR can measure ground deformation on the order of millimeters
- The south side of the Hilina Pali moves at a higher background rate
- The 2010 SSE deformation is mainly horizontal

## Correspondence to:

J. Chen,  
jingyi@stanford.edu

## Citation:

Chen, J., H. A. Zebker, P. Segall, and A. Miklius (2014), The 2010 slow slip event and secular motion at Kilauea, Hawai'i, inferred from TerraSAR-X InSAR data, *J. Geophys. Res. Solid Earth*, 119, doi:10.1002/2014JB011156.

Received 27 MAR 2014

Accepted 18 JUL 2014

Accepted article online 24 JUL 2014

## The 2010 slow slip event and secular motion at Kilauea, Hawai'i, inferred from TerraSAR-X InSAR data

Jingyi Chen<sup>1</sup>, Howard A. Zebker<sup>1,2</sup>, Paul Segall<sup>1</sup>, and Asta Miklius<sup>3</sup>

<sup>1</sup>Department of Geophysics, Stanford University, Stanford, California, USA, <sup>2</sup>Department of Electrical Engineering, Stanford University, Stanford, California, USA, <sup>3</sup>Hawaiian Volcano Observatory, U.S. Geological Survey, Hawaii Volcanoes National Park, Hawaii, USA

**Abstract** We present here a small baseline subset (SBAS) algorithm to extract both transient and secular ground deformations on the order of millimeters in the presence of tropospheric noise on the order of centimeters, when the transient is of short duration and known time and the background deformation is smooth in time. We applied this algorithm to study the 2010 slow slip event as well as the secular motion of Kilauea's south flank using 49 TerraSAR-X images. We also estimate the tropospheric delay variation relative to a given reference pixel using an interferometric synthetic aperture radar (InSAR) SBAS approach. We compare the InSAR SBAS solution for both ground deformation and tropospheric delays with existing GPS measurements and confirm that the ground deformation signal and tropospheric noise in InSAR data are successfully separated. We observe that the coastal region on the south side of the Hilina Pali moves at a higher background rate than the region north side of the Pali. We also conclude that the 2010 slow slip event (SSE) displacement is mainly horizontal and the maximum magnitude of the 2010 SSE vertical component is less than 5 mm.

### 1. Introduction

Since 1998, a sequence of slow slip events (SSEs) has been observed on the south flank of Kilauea, Hawaii, accompanied by swarms of small earthquakes [Cervelli *et al.*, 2002; Segall *et al.*, 2006; Brooks *et al.*, 2006; Wolfe *et al.*, 2007; Montgomery-Brown *et al.*, 2009, 2013]. One recent such SSE occurred on 1 February 2010. This event was first detected using continuous Global Positioning System (GPS) data, lasted at least 36 h, and resulted in centimeter-level displacements superimposed on long-term seaward background motion [Poland *et al.*, 2010]. Accurate measurement of ground motion due to SSEs facilitates the understanding of their mechanisms and potential relation to damaging earthquakes and flank failure [Moore *et al.*, 1989].

While high temporal resolution GPS measurements are widely used to study crustal deformations such as the 2010 SSE, interferometric synthetic aperture radar (InSAR) techniques [Rosen *et al.*, 2000; Hanssen, 2001] are also commonly used to measure surface motions [e.g., Massonnet *et al.*, 1993; Fialko *et al.*, 2002]. InSAR techniques have the advantage of achieving finer spatial resolution and broader ground coverage than is possible with GPS alone. Further, while the GPS measurements are more sensitive to horizontal motions, InSAR measurements are more sensitive to eastward and vertical motions as shown in section 2.3.

Shirzaei *et al.* [2013] jointly analyzed InSAR and GPS time series data from 2003 to 2010 using cluster and wavelet analyses and suggested that the long-term background motion on the south flank of Kilauea is focused on the Hilina and Holei Palis. In this paper, we focus on the transient 2010 SSE as well as the secular background motion at Kilauea using a modified InSAR small baseline subset (SBAS) approach [Bernardino *et al.*, 2002], which has been successfully used to monitor ground motion in many Earth science applications [e.g., Schmidt and Bürgmann, 2003; Lanari *et al.*, 2004; Hooper, 2008]. The challenge in using this algorithm for the present study is the very low signal-to-noise ratio (SNR), as tropospheric noise on Kilauea's south flank is typically on the order of centimeters or greater, comparable to the displacement during the SSE. We formulate the SBAS problem as joint GPS-InSAR inversion problem and successfully solve for transient and secular ground deformation with millimeter-level precision and 30 m × 30 m spatial resolution.

We also estimate the tropospheric delay variation relative to a given reference pixel using the InSAR SBAS method. Lauknes [2011] proposed a similar algorithm to estimate InSAR tropospheric stratification delays. Here we do not assume that the tropospheric delay is proportional to the surface elevation as this

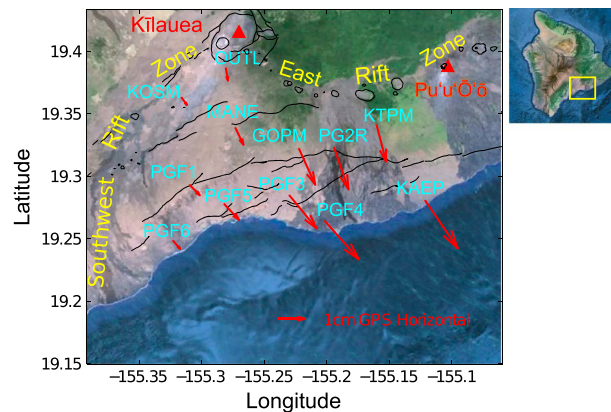


**Figure 1.** Map of Kilauea, Hawaii. The south flank of Kilauea is defined as the portion of Kilauea to the south of Kilauea’s caldera and its two rift zones. The horizontal displacements due to the 1 February 2010 slow slip event are shown as red arrows at the indicated GPS sites.

assumption may not be valid for the turbulent tropospheric processes characteristic of Hawaii. Instead, we interpret the InSAR data-fitting residual as tropospheric noise, based on the assumption that tropospheric noise is the dominant SBAS error source. Note that other factors such as inaccurate orbital or digital elevation model (DEM) information and nonmodeled deformation signals can also lead to InSAR measurement errors. In this study, we validate our assumption that tropospheric noise is much more significant than other error sources by showing that the tropospheric delays estimated from InSAR residual are consistent with independently measured zenith delay GPS data.

We use 49 TerraSAR-X SAR scenes acquired between August 2009 and December 2010 for this study. The TerraSAR-X satellite has a revisit cycle of 11 days—relatively short compared to most existing spaceborne radar systems. This shorter revisit cycle makes it possible to collect more measurements over a fixed period of time. Moreover, a phase cycle in a TerraSAR-X interferogram corresponds to only 1.55 cm line-of-sight (LOS) displacement, and the system is suitable for monitoring the ground deformation on the order of centimeters at Kilauea. Also, as the ionospheric delay is proportional to the square of the radar wavelength, X-band spaceborne radar systems ( $\lambda \sim 3$  cm) suffer from less severe ionospheric artifacts than many presently operating C-band ( $\lambda \sim 6$  cm) and L-band ( $\lambda \sim 24$  cm) spaceborne radar systems [Chen and Zebker, 2012].

In sections 2.1 and 2.2, we review previous studies of SSEs at Kilauea. We summarize how to measure ground motion using a single InSAR data pair in section 2.3 and how to solve for InSAR ground deformation time series using the SBAS approach in section 2.4. In section 3, we propose a modified SBAS algorithm to extract

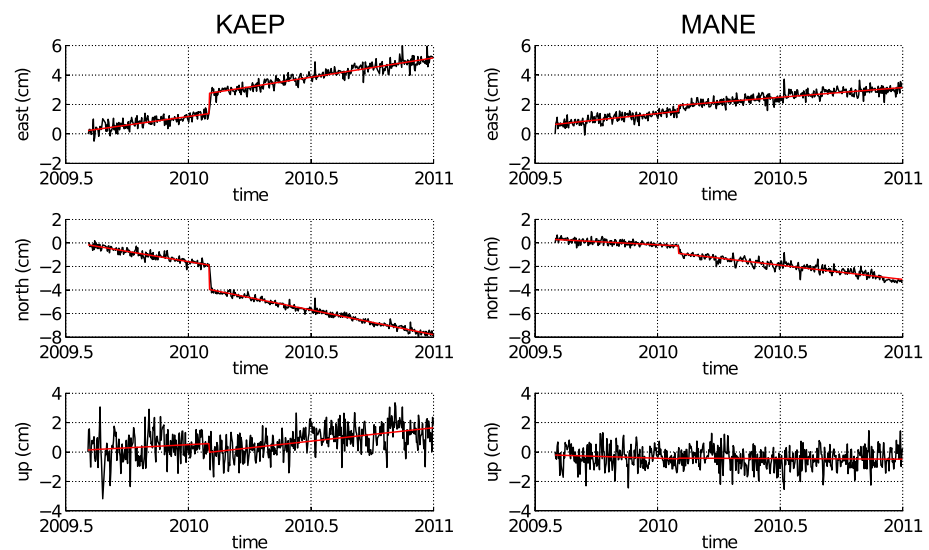


**Figure 2.** Daily GPS positions observed at the GPS stations (left) KAEP and (right) MANE from mid-2009 until the end of 2010 (in black). We fit two lines (in red) to the data before and after the slow slip event. The magnitude of the SSE can be inferred by the jump immediately before and after the event.

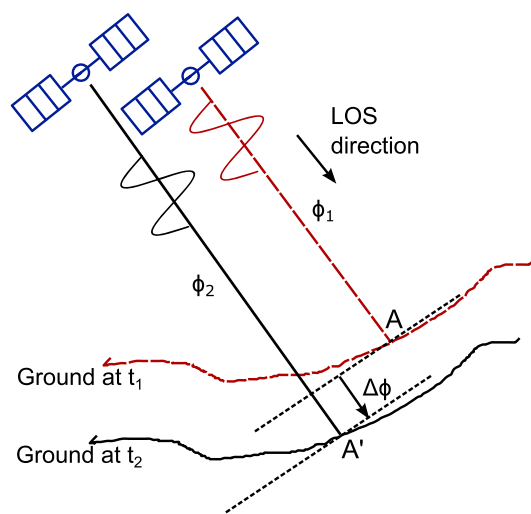


**Figure 3.** Illustration of InSAR imaging geometry. At time  $t_1$ , a ground pixel of interest is at point A and a radar satellite measures the phase  $\phi_1$  between the satellite and the ground pixel along the LOS direction. Later, at time  $t_2$ , the ground pixel has moved to A' and the satellite makes another measurement  $\phi_2$  between the satellite and the ground pixel. The phase difference  $\Delta\phi$  is proportional to the ground deformation between  $t_1$  and  $t_2$  along the LOS direction.

south flank. *Segall et al.* [2006] reported three SSEs on 20–21 September 1998, 3–4 July 2003, and 26–27 January 2005, all similar to the 2000 event. The SSEs at Kilauea are accompanied by swarms of small earthquakes located at depths of 7–8 km [*Segall et al.*, 2006; *Wolfe et al.*, 2007], constraining the location of the SSEs to the basal décollement [*Segall et al.*, 2006]. *Brooks et al.* [2006] analyzed 8 years of continuous GPS data and identified periodic SSEs between 1998 and 2005. All the SSEs have similar durations and displacement patterns, suggesting that they have a common source. *Montgomery-Brown et al.* [2009] compared displacement fields on Kilauea's south flank with displacement patterns in previously identified slow slip events. Matching displacement patterns were found for several new smaller candidate events between 1997 and 2007. *Brooks et al.* [2008] noted that a dike intrusion occurred a few hours before the 2007 slow slip event, suggesting that the intrusion triggered the 2007 SSE. The most recent 2010 and 2012 SSEs [*Poland et al.*, 2010; *Montgomery-Brown et al.*, 2013] are larger than the previous large events in 1998, 2000, 2005, and 2007. However, no corresponding dike intrusion was associated with either of the other events.

Unlike many SSEs previously observed at plate boundary subduction zones, such as southwestern Japan [*Hirose et al.*, 1999], Cascadia on the western coast of the USA and Canada [*Dragert et al.*, 2004], and Guerrero in southern Mexico [*Larson et al.*, 2004], *Montgomery-Brown et al.* [2013] reported that no associated tectonic tremor was detected during Kilauea's SSEs, suggesting that these SSEs reflect somewhat distinct slip processes compared to those at plate boundary subduction zones.

It has been over 10 years since the discovery of Kilauea's SSEs; however, the mechanisms behind these SSEs are still poorly understood. High spatial resolution and accurate InSAR SSE displacement measurements, while not modeled in this paper, constitute an important resource for studying the depth and lateral extent of the slip plane and may help to elucidate SSEs' potential relation to earthquakes and flank failure.

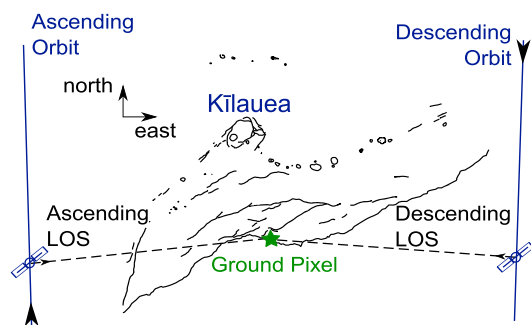


**Figure 4.** InSAR imaging geometry (plan view) with both ascending and descending radar passes over Kilauea's south flank.

both transient and secular ground deformations on the order of millimeters. In section 4, we apply this algorithm to study the 2010 slow slip event as well as the secular motion at Kilauea. In section 5, we describe an InSAR SBAS algorithm to estimate the relative tropospheric zenith delay. We then apply this algorithm to reconstruct the tropospheric zenith delay time series from TerraSAR-X data we processed.

## 2. Background

### 2.1. The Slow Slip Events at Kilauea, Hawaii

*Cervelli et al.* [2002] first recognized a transient southeastward displacement occurring on the south flank of Kilauea in November 2000 using continuous Global Positioning System (GPS) data. The event lasted about 36 h and resulted in a maximum of 1.5 cm seaward displacement. This event was an episode of aseismic fault slip called a slow slip event (SSE), which can be interpreted as fault activity somewhere between steady sliding and a dynamic earthquake.

Since the discovery of the 2000 SSE at Kilauea, a sequence of SSEs has been identified on Kilauea's

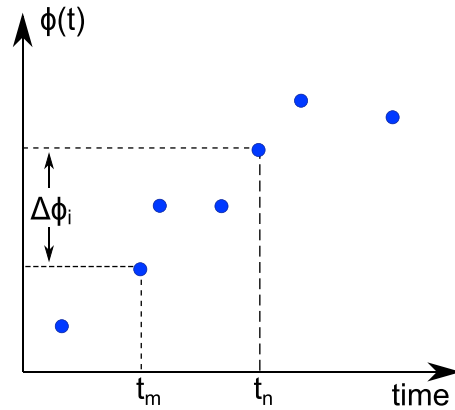


**Figure 5.** An LOS phase history at a given ground pixel location. The phase in a single interferogram formed from SAR data acquired at  $t_m$  and  $t_n$  yields  $\Delta\phi_i$ .

tectonic extension along the two rift zones and gravitational spreading. We fit two lines (in red) to the GPS data before and after the SSE. The magnitude of the SSE can be inferred by the jump immediately before and after the event. The magnitude of the SSE is much smaller at the inland station MANE compared to the coastal station KAEP. Note that the GPS vertical measurements are noisier than the horizontal measurements because of the GPS data acquisition geometry and trade-off with the tropospheric zenith delay [Misra and Enge, 2006].

### 2.3. Measuring Ground Motion Using InSAR

Figure 3 illustrates the InSAR imaging geometry. At time  $t_1$ , a ground pixel of interest is at point A and a radar satellite measures the phase  $\phi_1$  between the satellite and the ground pixel along the LOS direction. Later, at time  $t_2$ , the ground pixel has moved to A' and the satellite makes another measurement  $\phi_2$  between the satellite and the ground pixel. After removing the known phase  $\phi'$  due to the surface topography, the unwrapped InSAR phase  $\Delta\phi = \phi_2 - \phi_1 - \phi'$  is proportional to the ground deformation  $\Delta d$  between  $t_1$  and  $t_2$  along the satellite LOS direction as

$$\Delta\phi = \phi_2 - \phi_1 - \phi' = \frac{4\pi}{\lambda} \Delta d \quad (1)$$

where  $\lambda$  is the radar wavelength.

While InSAR techniques only measure one-dimensional LOS motion, it would be useful to characterize deformation in three dimensions: east, north, and up. Given the LOS direction unit vector  $e = [e_1, e_2, e_3]$ , we can project the deformation in east, north, and up (ENU) coordinates along the LOS direction as

$$\Delta d = e_1 \Delta d_{\text{east}} + e_2 \Delta d_{\text{north}} + e_3 \Delta d_{\text{up}} \quad (2)$$

Here we compute the LOS direction unit vector in the local ENU coordinates using satellite position files and the center ground pixel location.

The radar satellite usually obtains data over a single area from both ascending and descending passes as shown in Figure 4. We next use the TerraSAR-X data over Kilauea to illustrate how to infer the east and vertical components of the ground deformation by combining ascending and descending LOS measurements. The ascending LOS unit vector of the TerraSAR-X data we processed is approximately  $[0.5318, 0.0996, -0.8410]$  and the descending LOS unit vector is approximately  $[-0.5137, 0.0935, -0.8529]$ . Based on equation (2), we have

$$\begin{aligned} \Delta d_{\text{ascd}} &= 0.5318 \Delta d_{\text{east}} + 0.0996 \Delta d_{\text{north}} \\ &\quad - 0.841 \Delta d_{\text{up}} + \Delta n_{\text{ascd}} \\ \Delta d_{\text{descd}} &= -0.5137 \Delta d_{\text{east}} + 0.0935 \Delta d_{\text{north}} \\ &\quad - 0.8529 \Delta d_{\text{up}} + \Delta n_{\text{descd}} \end{aligned} \quad (3)$$

Here  $\Delta n_{\text{ascd}}$  represents noise in ascending LOS ground deformation measurement  $\Delta d_{\text{ascd}}$  and  $\Delta n_{\text{descd}}$  represents noise in descending LOS ground deformation measurement  $\Delta d_{\text{descd}}$ .

### 2.2. The 2010 Slow Slip Event at Kilauea, Hawaii

Figure 1 shows a map of Kilauea, the youngest and most active volcano on island of Hawai'i. It has a large summit caldera and two rift zones, in which a series of fissure vents allow lava to erupt with little explosive activity. Kilauea's south flank is defined as the portion of Kilauea to the south of Kilauea's caldera and its two rift zones, where the 2010 SSE started on 1 February of that year. The horizontal displacements of the event are shown as red arrows at the indicated GPS stations in Figure 1. Here we estimate the magnitude of the SSE displacements from the daily GPS position time series at each GPS station. As an example, Figure 2 shows the east, north, and up components of the daily GPS position at two GPS stations KAEP and MANE from mid-2009 until the end of 2010 (in black). The transient SSE signal can be seen superimposed on an approximately linear seaward background motion. This background motion is due to

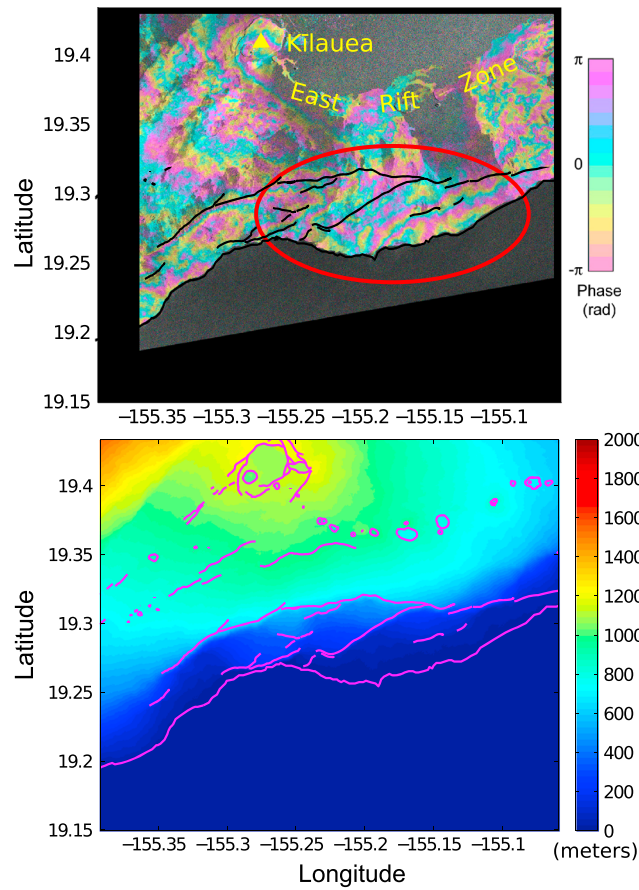


**Figure 6.** (top) A single interferogram formed from ascending TerraSAR-X data acquired on 3 March and 7 January 2010. A phase cycle  $2\pi$  in the wrapped interferogram corresponds to 1.55 cm LOS deformation. We expect to observe a phase signature due to the SSE in the red circled area, but the expected SSE phase signature is obscured by significant artifacts presumed to be due to tropospheric noise. (bottom) The terrain elevation map (in meters) of Kilauea's south flank as obtained from the Shuttle Radar Topography Mission (SRTM). We use SRTM data to flatten the interferograms.

motion at Kilauea. Here we review how this algorithm solves for the InSAR phase time series at a ground pixel location.

Suppose we want to solve for the unknown LOS phase history  $\phi(t)$  at a ground pixel as shown in Figure 5. The  $i$ th interferogram formed from two SAR scenes acquired at  $t_m$  and  $t_n$  measures the unwrapped phase  $\Delta\phi_i$  at this pixel. We can write  $\Delta\phi_i$  as

$$\Delta\phi_i = \sum_{l=m}^{n-1} (t_{l+1} - t_l) v_l \quad (6)$$

where  $v_l$  is the unknown mean LOS velocity (in rad/d) between SAR acquisition times  $t_l$  and  $t_{l+1}$ .

An interferogram can measure  $\Delta\phi_i$  in equation (6) with negligible topographic or spatial decorrelation noise only if the baseline (the spatial separation between the satellite locations at two SAR acquisition times) is small [Zebker and Villasenor, 1992]. Given  $N$  SAR images forming  $M$  interferograms with small baselines, we can define a matrix representation of the  $M$  equation SBAS system as

$$Bv = \Delta\tilde{\Phi} \quad (7)$$

Combining the ascending and descending LOS measurements leads to

$$\begin{aligned} \Delta d_{\text{east}} &= 0.9631\Delta d_{\text{ascd}} - 0.9496\Delta d_{\text{descd}} \\ &\quad - 0.0071\Delta d_{\text{north}} - 0.9631\Delta n_{\text{ascd}} \\ &\quad + 0.9496\Delta n_{\text{descd}} \\ \Delta d_{\text{up}} &= -0.5801\Delta d_{\text{ascd}} - 0.6005\Delta d_{\text{descd}} \\ &\quad + 0.1139\Delta d_{\text{north}} + 0.5801\Delta n_{\text{ascd}} \\ &\quad + 0.6005\Delta n_{\text{descd}} \end{aligned} \quad (4)$$

We can estimate east and vertical components of the ground deformation as

$$\begin{aligned} \Delta d_{\text{east}} &\approx 0.9631\Delta d_{\text{ascd}} - 0.9496\Delta d_{\text{descd}} \\ \Delta d_{\text{up}} &\approx -0.5801\Delta d_{\text{ascd}} - 0.6005\Delta d_{\text{descd}} \end{aligned} \quad (5)$$

Because the observations are less sensitive to the north component of displacement, we neglect the terms  $\Delta d_{\text{north}}$ ,  $\Delta n_{\text{ascd}}$ , and  $\Delta n_{\text{descd}}$  in equation (4). Suppose  $\Delta d_{\text{north}}$  equals 1 cm. The error due to  $\Delta d_{\text{north}}$  in the east ground deformation estimate is less than 0.1 mm, and the error due to  $\Delta d_{\text{north}}$  in the vertical ground deformation estimate is approximately 1 mm.

#### 2.4. InSAR Time Series Analysis Using Small Baseline Subset Method

Berardino *et al.* [2002] proposed the small baseline subset (SBAS) algorithm for monitoring the temporal evolution of surface deformation. We use the SBAS method to extract the ground deformation signals for the transient 2010 SSE and the secular background

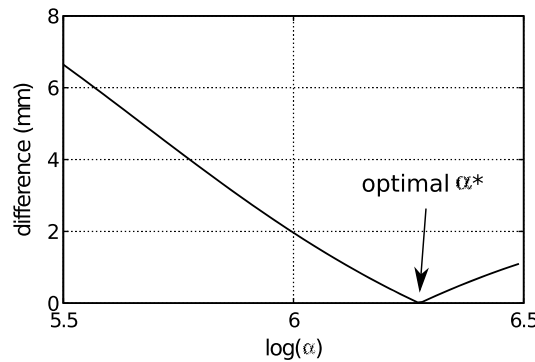


**Figure 7.**  $|\Delta d_{\text{GPS}} - \Delta d_{\text{InSAR}}|$  along ascending LOS direction as a function of  $\log(\alpha)$ . Here  $\Delta d_{\text{GPS}}$  is defined in equation (10) and  $\Delta d_{\text{InSAR}}$  is defined in equation (11).

LOS phase history  $\phi(t)$  at the pixel of interest. We can then resample the descending LOS time series based on the ascending data acquisition times and further infer the east and vertical components of the ground deformation, as described in section 2.3.

### 3. Algorithm

We propose an SBAS InSAR time series analysis algorithm to extract both transient and secular ground deformations at Kīlauea. The challenge here is the very low SNR, as the SSE signal is much below the tropospheric noise level. For example, Figure 6 (top) is a single interferogram formed from two ascending TerraSAR-X scenes acquired on 7 January and 3 March 2010, over Kīlauea’s south flank. We have removed the topography-related phase using the digital elevation model (DEM) as shown in Figure 6 (bottom) obtained from the Shuttle Radar Topography Mission (SRTM). Based on GPS data, the 1 February 2010 Kīlauea SSE was associated with an approximately 7 mm maximum deformation along the TerraSAR-X ascending LOS direction, and we would expect to observe a phase signature due to the SSE in the red circled area. However, since the tropospheric noise is typically on the order of centimeters or greater at Kīlauea [Foster et al., 2006], the expected SSE phase signature is obscured by significant tropospheric noise.

Due to the low SNR, traditional SBAS results may not accurately represent the ground motion if some effort is not made to handle or suppress the tropospheric noise. As the spatial variations of the SSE signal and tropospheric noise are very similar, applying a tropospheric filter on the interferograms tends to smooth both the transient SSE signal and tropospheric noise at the same time. Instead of applying the tropospheric filter directly in the data domain, we employ a simple ground deformation model consisting of an offset at the time of the SSE superimposed on constant velocity background motion. To prevent overfitting

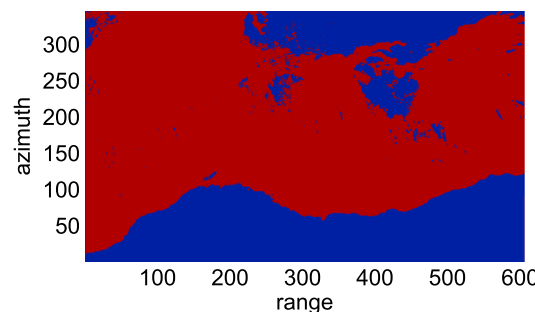


**Figure 8.** The mask we use for ascending TerraSAR-X interferograms. The horizontal axis corresponds to the radar range direction, and the vertical axis corresponds to the radar azimuth direction. Pixels with low-correlation values ( $< 0.1$ ) are marked in blue, and pixels with high-correlation values ( $\geq 0.1$ ) are marked in red.

where  $v = [v_1 \dots v_{N-1}]^T$  is the vector of unknown mean velocities between each consecutive SAR acquisition and  $\Delta\Phi = [\Delta\phi_1 \dots \Delta\phi_M]^T$  is the vector of known LOS values of the  $M$  interferograms at the given pixel. The  $M \times (N - 1)$  matrix  $B$  is the SBAS matrix. If the  $i$ th interferogram measures the InSAR phase  $\Delta\phi_i$  between SAR data acquisition times  $t_m$  and  $t_n$  as defined in equation (6) at the pixel of interest, the  $i$ th row of  $B$  has  $\Delta t_l = (t_{l+1} - t_l)$  in the  $l$ th entry for  $l = m, \dots, (n - 1)$  and zeros in the remaining entries.

The vector  $v$  in equation (7) can be estimated using, for example, the singular value decomposition (SVD) as described in Berardino et al. [2002]. An additional integration step yields the

in particularly noisy regions, we formulate the problem as a joint GPS-InSAR inversion and solve for the phase history at all interferogram pixels simultaneously with a spatial smoothness constraint on the offset. Note that here we apply the spatial smoothness constraint in the model domain. Smoothing of the background velocity is not necessary, as the linear background motion model tolerates random noise well.

We define the pixel at  $i$ th range bin and  $j$ th azimuth line in a 2-D interferogram as the  $k$ th pixel, where  $k = [(i - 1)n_r + j]$  and  $n_r$  is the total number of range bins in the interferogram. Given  $N$  SAR images forming  $M$  small baseline interferograms, we can solve for the unknown ground motion in the LOS

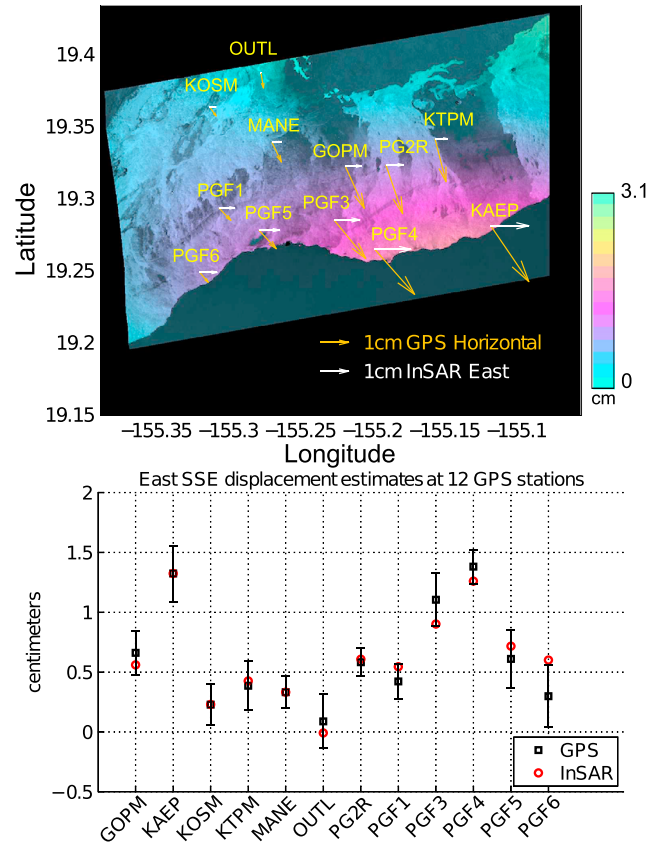


**Figure 9.** (top) Map of the east displacement field due to the 2010 SSE at Kilauea as derived from TerraSAR-X data. The white arrows illustrate the magnitude of the SSE east displacement at each of the 12 GPS stations (labeled in yellow) as estimated from InSAR data. For comparison, the dark yellow arrows illustrate the magnitude of the SSE horizontal displacement at these locations as estimated from GPS data. (bottom) InSAR (in red) and GPS (in black) estimates of the east SSE displacement at 12 GPS sites. The error bar indicates the 95% confidence limits of the GPS measurements.

equation (8). The number of diagonal block entries in  $G$  equals the number of pixels  $n_p$  in one interferogram. The unknown model vector  $m = [m^{(1)} \dots m^{(n_p)}]^T$  and the data vector  $\Delta\Phi = [\Delta\Phi^{(1)} \dots \Delta\Phi^{(n_p)}]^T$ , where the  $k$ th entry in  $m$  and  $\Delta\Phi$  are also defined in equation (8). The matrix  $D$  is constructed such that  $\|Dm\|_2^2 = \|D_r\delta\|_2^2 + \|D_a\delta\|_2^2$ , where  $D_r$  and  $D_a$  are matrices that compute discrete approximations to the derivatives in the range and azimuth directions. The vector  $\delta$  consists of only the offset part of the solution vector  $m$ , that is,  $\delta = [\delta^{(1)}, \delta^{(2)}, \dots, \delta^{(n_p)}]^T$ . Note that the regularization term does not apply to the velocity solution  $v$ .

The regularization parameter  $\|Dm\|_2^2$  penalizes large spatial gradients in the reconstructed offset solutions. When the damping parameter  $\alpha$  is too small, the solution suffers from overfitting. On the other hand, when  $\alpha$  is too large, the solution suffers from excessive smoothing. We determine the optimal damping parameter  $\alpha^*$  heuristically using GPS data from two GPS stations KAEP and MANE. We select KAEP and MANE as our reference sites because InSAR only measures relative motions between pixels, and the SSE signal is much more significant at KAEP than at MANE (as discussed in section 2.2).

We denote the magnitude of the SSE in east, north, and up coordinates as  $d_K = [E_1 \ N_1 \ U_1]$  at KAEP and  $d_M = [E_2 \ N_2 \ U_2]$  at MANE. We project the difference between  $d_K$  and  $d_M$  to the LOS direction as

$$\Delta d_{\text{GPS}} = e_1(E_1 - E_2) + e_2(N_1 - N_2) + e_3(U_1 - U_2) \quad (10)$$

where  $e = [e_1, e_2, e_3]$  is the InSAR LOS direction unit vector.

direction at the  $k$ th pixel by minimizing the squared error as

$$\|G^{(k)}m^{(k)} - \Delta\Phi^{(k)}\|_2^2 \quad (8)$$

Here the  $2 \times 1$  vector  $m^{(k)} = [v^{(k)} \ \delta^{(k)}]^T$  is the unknown constant background velocity  $v^{(k)}$  (in rad/d) and jump  $\delta^{(k)}$  (in radians) due to the SSE in the LOS direction at the  $k$ th pixel. The  $M \times 2$  matrix  $G^{(k)} = [s \ c]$ . The linear SBAS vector  $s = BP$ , where the  $M \times (N - 1)$  matrix  $B$  is given by equation (7) and  $P$  is an  $(N - 1) \times 1$  vector of ones,  $[1 \dots 1]^T$ . Note that  $Pv^{(k)}$  equals  $[v^{(k)} \dots v^{(k)}]^T$ . The  $M \times 1$  vector  $c$  has a one in the  $l$ th entry if the  $l$ th interferogram spans the SSE. Otherwise, the  $l$ th entry of  $c$  equals zero. The  $M \times 1$  vector  $\Delta\Phi^{(k)} = [\Delta\phi_1^{(k)} \dots \Delta\phi_M^{(k)}]^T$  contains the unwrapped phase values of the  $M$  interferograms at the  $k$ th pixel.

Solving for the weak SSE signal at every pixel independently using the least squares method in equation (8) leads to a solution that overfits the tropospheric noise. To prevent overfitting, we introduce a spatial smoothness constraint on the offset estimate and solve for the phase history at all interferogram pixels simultaneously as a regularized least squares problem by minimizing

$$\|Gm - \Delta\Phi\|_2^2 + \alpha \|Dm\|_2^2 \quad (9)$$

Here  $G$  is block diagonal, where the  $k$ th diagonal block entry equals  $G^{(k)}$  in

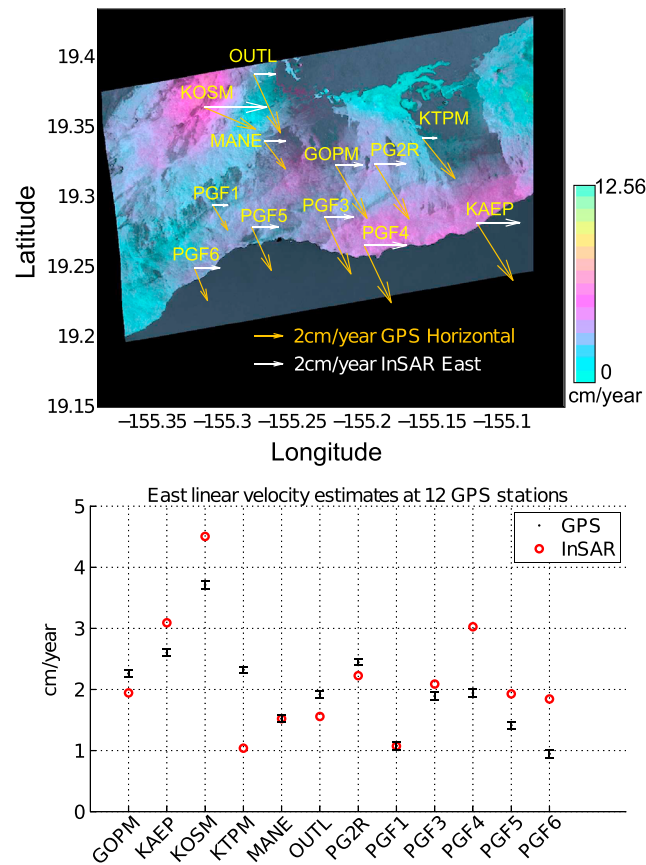


**Figure 10.** (top) Map of the east background velocity field at Kilauea as derived from TerraSAR-X data. The white arrows illustrate the magnitude of the east background velocity as estimated from InSAR data at each of the 12 GPS stations, while the dark yellow arrows illustrate the magnitude of the horizontal background velocity as estimated from GPS data at these locations. (bottom) InSAR and GPS estimates of the east background velocity at 12 GPS sites. The error bar indicates the 95% confidence limits of the GPS measurements.

that minimizes the root-mean-square (RMS) error of the InSAR SSE east component estimate at 12 available GPS stations in the area of interest. Additional GPS stations near the East Rift Zone are not included for this analysis, because the simple linear offset model does not represent the complex deformation due to rift zone volcanic activity.

#### 4. Results

We processed 24 ascending and 25 descending TerraSAR-X scenes acquired between August 2009 and December 2010. The image quality of the resulting 576 interferograms is comparable to Figure 6. All were included in the small baseline analysis with a maximum temporal separation of 473 days and a maximum perpendicular baseline of 339 m. We unwrapped the interferograms using Statistical-Cost, Network-Flow Algorithm for Phase Unwrapping (SNAPHU) [Chen and Zebker, 2002]. Since most of the study area is covered by rocks only, the coherence at these pixels is high and the phase unwrapping error is small. Pixels with low-correlation values ( $< 0.1$ ) due to water, vegetation, and active lava flow are masked out in the SBAS results. The mask we use for the ascending TerraSAR-X interferograms is shown in Figure 8, and the same mask is used for the descending interferograms.

In this section, we present the InSAR SBAS solutions for the ground deformation at Kilauea. Because InSAR techniques can only measure relative motions between pixels, we calibrate InSAR ground deformation results by a constant shift, which we derive from GPS data from the GPS station MANE.

Minimizing equation (9) for a given  $\alpha$ , we can compute an InSAR estimate of the magnitude of the SSE in the LOS direction, which we denote as  $\delta^{(K)}$  at KAEP and  $\delta^{(M)}$  at MANE. We define  $\Delta d_{\text{InSAR}}$  as

$$\Delta d_{\text{InSAR}} = \delta^{(K)} - \delta^{(M)} \quad (11)$$

We next compute  $|\Delta d_{\text{GPS}} - \Delta d_{\text{InSAR}}|$  for different values  $\alpha$ . Figure 7 shows  $|\Delta d_{\text{GPS}} - \Delta d_{\text{InSAR}}|$  as a function of  $\log(\alpha)$  for the ascending InSAR data. The optimal  $\alpha^*$  is the one that minimizes  $|\Delta d_{\text{GPS}} - \Delta d_{\text{InSAR}}|$ .

We process the ascending and descending InSAR data separately and then extract the east and vertical ground deformation by combining the ascending and descending LOS deformation estimate, as described in section 2.3. The noisy GPS vertical measurements lead to errors in the final InSAR solution because of errors in  $(U_1 - U_2)$  in equation (10). To improve the accuracy of our algorithm, we test many possible values  $\Delta \tilde{U}$  between  $(U_1 - U_2 - \epsilon)$  and  $(U_1 - U_2 + \epsilon)$ , where  $\epsilon$  is the GPS vertical measurement  $1\sigma$  uncertainty. We set  $\epsilon$  equals 5 mm. For each possible  $\Delta \tilde{U}$ , we compute  $\Delta \tilde{d}_{\text{GPS}} = [e_1(E_1 - E_2) + e_2(N_1 - N_2) + e_3 \Delta \tilde{U}]$  and the corresponding InSAR east and vertical ground deformation solution.

We select the optimal  $\Delta \tilde{U}$  as the one

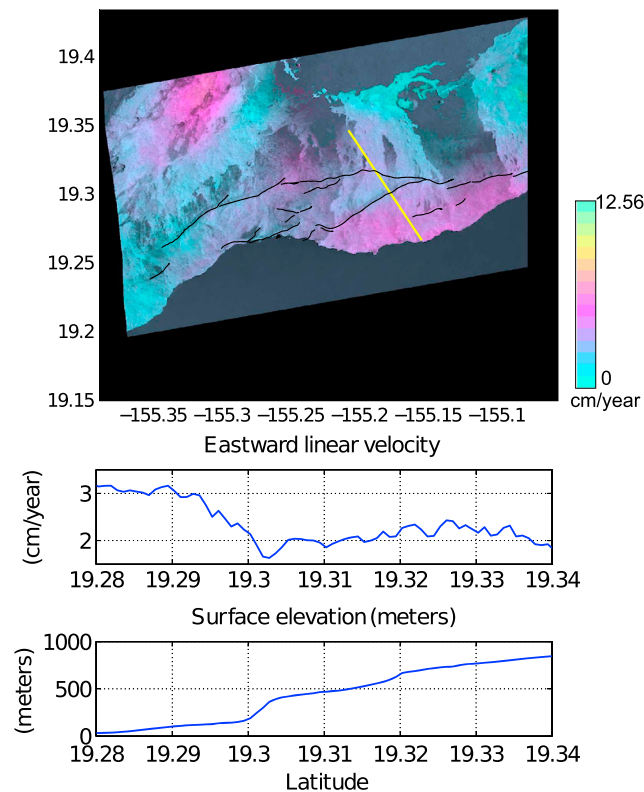


**Figure 11.** Profile of the east component of the background velocity and surface elevation across Kilauea's south flank. In the linear velocity map (top), we show the transect location in yellow and the major faults of the Hilina Fault System in black.

background velocity field at Kilauea and plot the InSAR and GPS east background velocity estimates at the 12 GPS sites, as shown in Figure 10. If we take the GPS measurements as ground truth, then the RMS error of the InSAR background velocity estimate at these 12 GPS sites is about 6.5 mm/yr. For comparison, the median east background velocity on the south flank of Kilauea is about 2 cm/yr. We next extract the InSAR east background velocity estimate along the yellow line illustrated in Figure 11. The east velocity profile in Figure 11 suggests that the coastal region on the south side of the Hilina Pali moves at a higher background rate than the region north side of the Pali. Note that we do not observe a jump in the InSAR SSE displacement estimate along the same profile. This may be because the spatial smoothness constraint we employ on the jump estimate would not preserve the discontinuity in the SSE solution.

We next reconstruct east InSAR deformation time series by integrating the linear velocity over time and imposing the estimated offset at the time of the SSE. We then compare the InSAR and GPS east ground deformation time series at 12 GPS stations as shown in Figure 12. Both GPS and InSAR time series are shifted to zero mean. The differences between the InSAR and GPS measurements at most GPS sites are on the order of millimeters. The estimation error may be due to the following reasons. First, although the spatial smoothness constraint on the SSE displacement estimate prevents overfitting in noisy regions, the residual tropospheric noise is also spatially correlated and cannot be removed completely using our algorithm. Furthermore, the coastal GPS stations are farther away from the reference location MANE. As a result, the tropospheric noise at these GPS sites is less correlated with the tropospheric noise at the reference location, which leads to larger InSAR SBAS estimation errors at locations such as the GPS site PGF6. Second, we assume the background motion is linear in time. This assumption may not be valid over a long period of time, especially near Kilauea caldera due to additional source of magmatic deformation. Third, decorrelation of X-band interferometry over vegetated areas is another cause of estimation errors at pixel locations such as the GPS site KTPM. Fourth, other factors such as inaccurate orbital or DEM information and nonmodeled deformation signals can also lead to SBAS data-fitting errors. However, we demonstrate that these error sources are less significant comparing to tropospheric noise in section 5.

#### 4.1. East Component of Ground Motion

The InSAR SSE estimate at a given pixel  $k$  is the solution for the jump  $\delta^{(k)}$  in our model  $m^{(k)}$  as defined in equation (8). We compute a map of the east displacement field due to the 2010 SSE at Kilauea using TerraSAR-X data and plot the InSAR (in red) and GPS (in black) east SSE displacement estimates at these 12 GPS sites, as shown in Figure 9. Here we compute the GPS SSE east displacement as the difference between the GPS 10 day average displacement before and after the SSE. If we take the GPS SSE estimate as ground truth, then the RMS error of the InSAR east SSE estimate at these 12 GPS sites is about 1.3 mm. As a comparison, the east displacement due to the 2010 SSE is on the order of centimeters. In spite of the fact that tropospheric noise in the Kilauea region is also on the order of centimeters, our algorithm achieves millimeter-level accuracy in the east component.

The InSAR background velocity estimate at a given pixel  $k$  is the solution for  $v^{(k)}$  in our model  $m^{(k)}$  as defined in equation (8).

We compute a map of the InSAR east

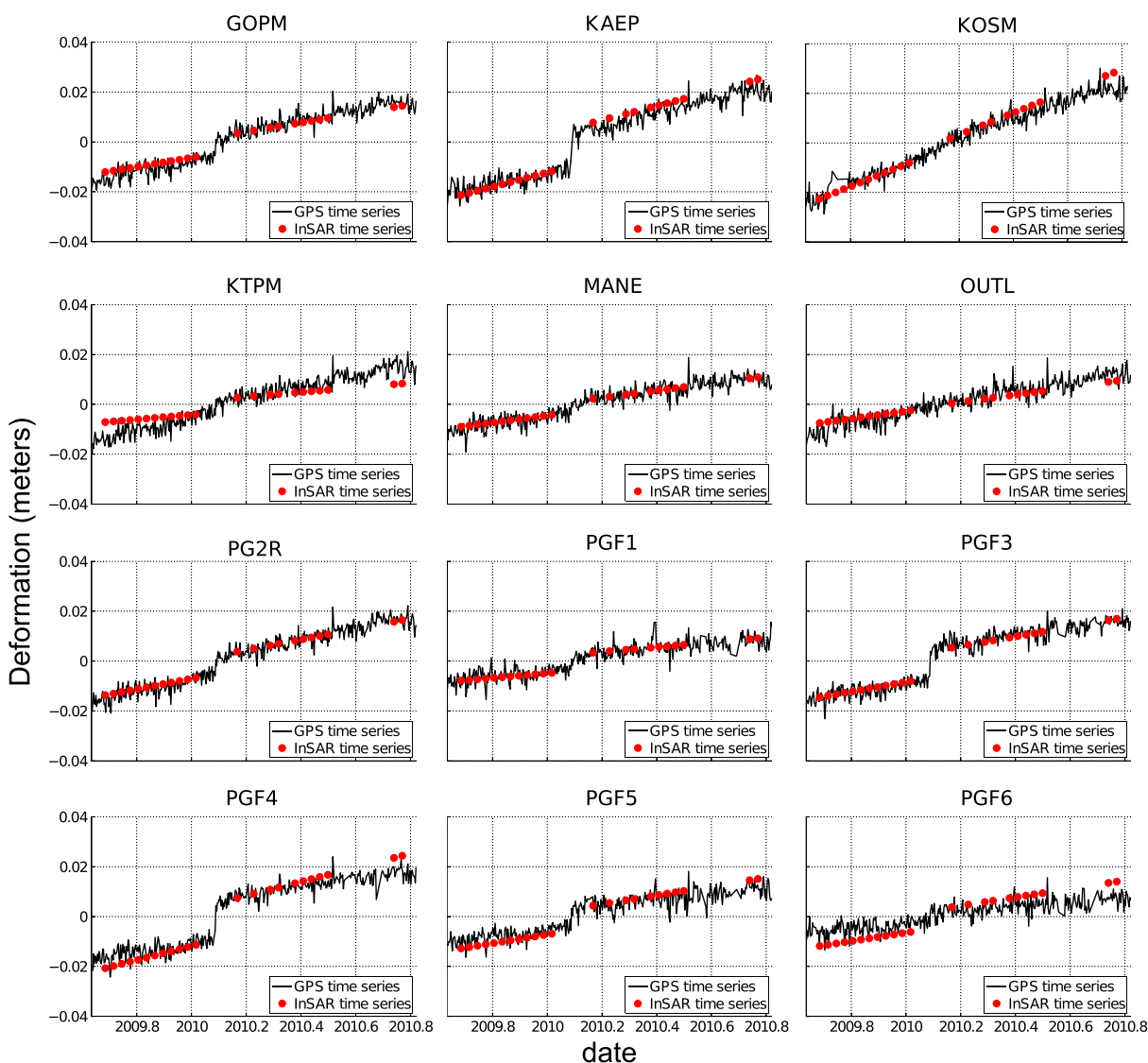


**Figure 12.** East ground deformation time series estimated from GPS data (in black) and InSAR data (in red) at 12 GPS stations on the south flank of Kilauea. Both GPS and InSAR time series are shifted to zero mean. The jump in the InSAR time series corresponds to the 2010 slow slip event east displacement, and the slope of the linear motion corresponds to the east background velocity.

#### 4.2. Up Component of Ground Motion

Figure 13 shows a map of the vertical displacement field due to the 2010 SSE. Because the GPS vertical time series are very noisy, we do not take the GPS vertical SSE estimate as ground truth. To calibrate the InSAR results, we assume that there is no vertical SSE displacement at the GPS site MANE. This assumption is consistent with GPS observations at MANE as shown in Figure 2. We plot the InSAR (in red) and GPS (in black) vertical SSE displacement estimates at 12 GPS sites. Both GPS and InSAR measurements suggest that the magnitude of the 2010 SSE vertical component is much smaller than the SSE east component. The relative errors between the GPS and InSAR vertical SSE estimates are larger than those for the east estimates, with an RMS error at the 12 GPS sites of about 5 mm. Note that GPS data at coastal stations PGF3 and PGF4 suggest that the SSE causes subsidence. However, InSAR data in the same region suggest that the SSE leads to uplift. The difference may be due to the following reasons. First, the uncertainty in the GPS vertical measurement is about 5 mm [Montgomery-Brown *et al.*, 2009] and the noise in the GPS data prevents a better comparison with InSAR data. Second, residual tropospheric noise causes errors in the InSAR estimate. Equation (4) in section 2.3 suggests that tropospheric noise causes different artifacts in InSAR east and vertical SSE estimates. Third, equation (4) indicates that neglecting the centimeter-level SSE southward displacement can

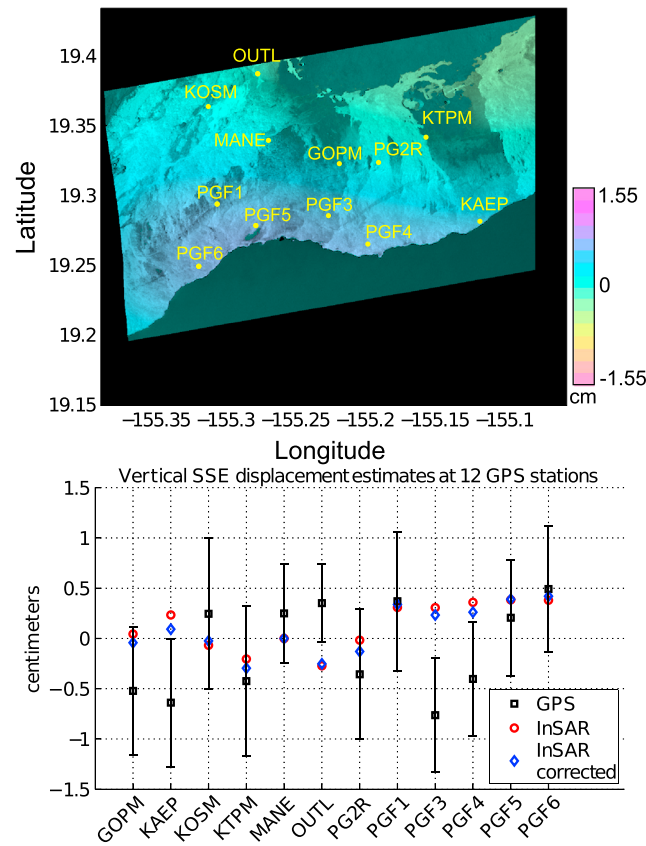


**Figure 13.** (top) Map of the vertical displacement field due to the 2010 SSE at Kilauea as derived from TerraSAR-X InSAR data. To calibrate the InSAR results, we assume that there is no vertical displacement due to the SSE at the GPS site MANE. (bottom) InSAR (in red) and GPS (in black) estimates of the vertical SSE displacement at 12 GPS sites. We also correct the error in InSAR vertical displacement estimate due to the SSE southward motion using GPS data as shown in blue. The error bar indicates the 95% confidence limits of the GPS measurements.

direction due to the 2010 SSE, the InSAR and GPS estimates of the long-term vertical motion are consistent and have millimeter accuracy.

### 5. Estimating the Tropospheric Noise in InSAR Data

We next demonstrate how to use InSAR data to estimate the variation in tropospheric delay relative to a given reference pixel. Here the algorithm is based on the assumption that tropospheric noise is the dominant SBAS error source. For this study, we validate our assumption by the following two steps. First, we inspect every interferogram and verify that there are no obvious phase artifacts due to phase unwrapping, DEM, and orbital errors. Second, we compare the relative tropospheric zenith delays as estimated from InSAR residual and GPS zenith delay data and demonstrate these that two independent measurements are consistent. The algorithm and results are presented as follows.

We define the LOS tropospheric phase delay (in radians) at a pixel of interest  $k$  and  $N$  SAR data acquisition times as an  $N \times 1$  vector  $x^{(k)} = [x_1^{(k)} \dots x_N^{(k)}]^T$  and the LOS tropospheric phase delays (in radians) at the InSAR reference pixel  $r$  and  $N$  SAR data acquisition times as an  $N \times 1$  vector  $x^{(r)} = [x_1^{(r)} \dots x_N^{(r)}]^T$ . The relative LOS tropospheric phase delays at the pixel  $k$  are then defined as  $\Delta x^{(k)} = x^{(k)} - x^{(r)}$ .

We write the InSAR data residual vector  $\Delta\Phi_{\text{res}}^{(k)}$  at the pixel  $k$  as

$$\Delta\Phi_{\text{res}}^{(k)} = \Delta\Phi^{(k)} - G^{(k)}m^{(k)} \tag{12}$$

lead to millimeter-level errors in the InSAR vertical SSE estimate. We can correct this error using GPS data at the 12 GPS sites, as shown in blue in Figure 13; however, the low-resolution GPS data are not sufficient for correcting the InSAR vertical displacement field over the entire south flank of Kilauea.

Figure 14 shows a map of the vertical background velocity field at Kilauea. Here we also assume that there is no vertical background motion at GPS site MANE in order to calibrate the InSAR results. We plot the InSAR and GPS estimates of the vertical background velocity at 12 GPS sites in the same figure. The GPS and InSAR ground deformation measurements are consistent at all 12 GPS sites, and the root-mean-square difference of the GPS and InSAR estimate is about 3.8 mm/yr. For comparison, the median vertical background velocity relative to GPS site MANE is about 1 cm/yr.

We reconstruct the vertical ground deformation history using the InSAR SBAS solution. We then compare the InSAR and GPS vertical ground motion time series at the 12 GPS stations as shown in Figure 15. While there is no clear jump in the vertical

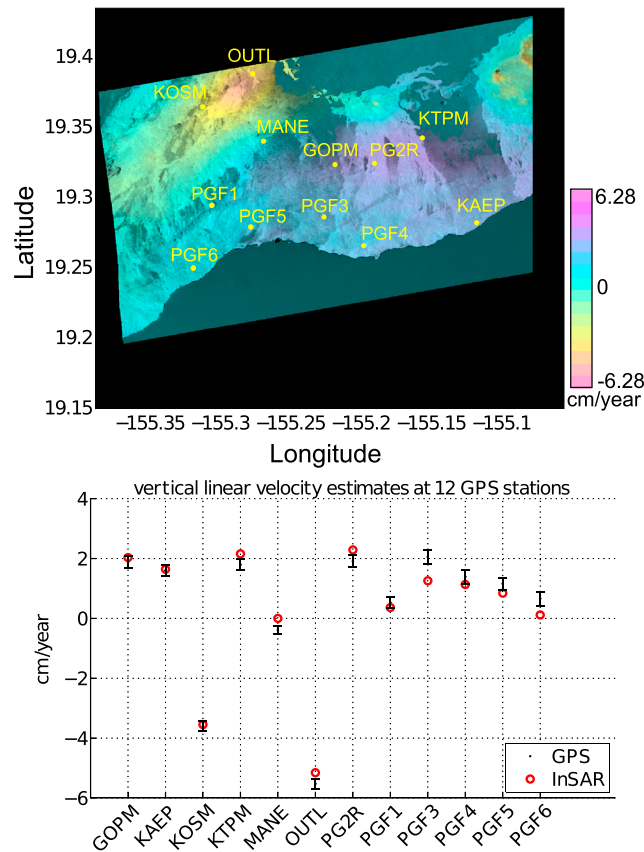


**Figure 14.** (top) Map of the vertical background velocity field at Kilauea as derived from TerraSAR-X InSAR data. To calibrate the InSAR results, we assume that there is no vertical background motion at the GPS site MANE. (bottom) InSAR and GPS estimates of the vertical background velocity at 12 GPS sites. The error bar indicates the 95% confidence limits of the GPS measurements.

The vector  $\Delta x^{(k)}$  in equation (13) can be estimated using, for example, the SVD as in section 2.4. We then compute the relative tropospheric zenith delays (in meters) as

$$\Delta \bar{x}^{(k)} = \frac{4\pi}{\lambda} \Delta x^{(k)} e_3 \quad (14)$$

where  $\lambda$  is the radar wavelength in meters and  $e_3$  is the vertical component of the LOS direction unit vector  $e = [e_1, e_2, e_3]$ .

To test the algorithm we present here, the GPS data for the same time period are also analyzed to estimate tropospheric zenith delays using the GPS Inferred Positioning System-Orbit Analysis Simulation Software package. We define the GPS tropospheric zenith delay estimates at a GPS station of interest  $s$  and  $N$  SAR acquisition times as  $y^{(s)} = [y_1^{(s)} \dots y_N^{(s)}]^T$  and the GPS zenith delay estimates at the reference GPS station  $r$  and  $N$  SAR acquisition times as  $y^{(r)} = [y_1^{(r)} \dots y_N^{(r)}]^T$ . The relative zenith delays at the GPS station  $s$  are then defined as  $\Delta y^{(s)} = y^{(s)} - y^{(r)}$ , which we compare directly with InSAR relative zenith delay estimates.

Figure 16 shows the relative tropospheric zenith delays as estimated from ascending InSAR data (in red) and GPS data (in black) at 11 Kilauea GPS stations. Here we select the GPS station MANE as the reference station for processing InSAR and GPS data. Similarly, Figure 17 shows the relative tropospheric zenith delays as estimated from descending InSAR data (in red) and GPS data (in black) at these stations. The correlation coefficients between the InSAR- and GPS-driven tropospheric delay time series are given in blue for each station. The GPS- and InSAR-driven delay time series are well correlated. This confirms that InSAR noise is largely due to tropospheric noise and the ground deformation signal and tropospheric noise in InSAR data

Here  $G^{(k)}$ ,  $m^{(k)}$ , and  $\Delta\Phi^{(k)}$  are defined in equation (8). The size of  $\Delta\Phi_{\text{res}}^{(k)}$  is  $M \times 1$ , where  $M$  is the total number of interferograms. The  $i$ th entry in  $\Delta\Phi_{\text{res}}^{(k)}$  corresponds to the difference between the observed phase value at the  $k$ th pixel of the  $i$ th interferogram and the fitted phase value provided by the linear-plus-offset model, as described in section 3.

Suppose the  $i$ th interferogram is formed using two SAR scenes acquired at  $t_m$  and  $t_n$ . If SBAS data-fitting errors are mainly due to tropospheric noise, the  $i$ th entry in  $\Delta\Phi_{\text{res}}^{(k)}$  approximately represents the relative LOS tropospheric phase delay difference ( $\Delta x_m^{(k)} - \Delta x_n^{(k)}$ ). We can solve for the relative LOS tropospheric phase delays at  $N$  SAR data acquisition times using  $M$  interferograms ( $M > N$ ). The matrix representation of the overdetermined system is

$$A \Delta x^{(k)} = \Delta\Phi_{\text{res}}^{(k)} \quad (13)$$

Here  $A$  is an  $M \times N$  matrix corresponding to the SAR scene indices used to form the interferograms. Given that the  $i$ th interferogram is formed using SAR data acquired at  $t_m$  and  $t_n$ , the  $i$ th row in  $A$  has a one in the  $m$ th entry, a minus one in the  $n$ th entry and zeros in the remaining  $N - 2$  entries.

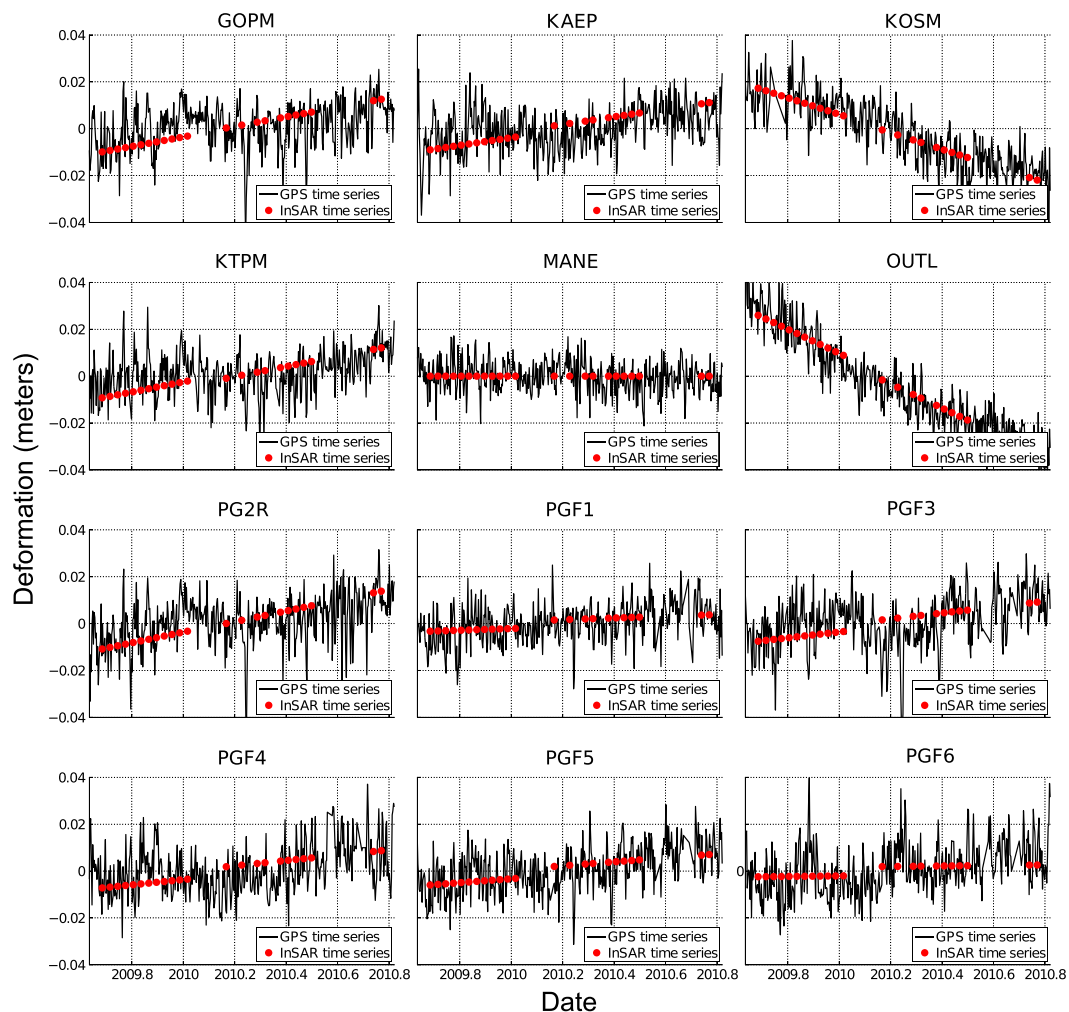


**Figure 15.** Vertical ground deformation time series estimated from GPS data (in black) and InSAR data (in red) at 12 GPS stations on the south flank of Kilauea. Both GPS and InSAR time series are shifted to zero mean. There is no clear jump in vertical deformation due to the 2010 SSE.

are successfully separated. The mismatch between the InSAR- and GPS-driven tropospheric delay time series may be due to other InSAR measurement errors such as orbital errors and nonmodeled deformation signals. Errors in GPS zenith delay estimates can also lead to low-correlation values at some stations such as KOSM.

We also compute the standard deviation (SD) of the relative tropospheric noise time series vector  $\Delta\tilde{x}^{(k)}$  in equation (14) for every InSAR pixel  $k$ . Figure 18 shows the resulting tropospheric noise temporal standard deviation map as derived from ascending and descending TerraSAR-X interferograms. The major faults in the Hilina Fault System are marked with black lines. We observe that there is a jump in the SD values at locations where major faults are crossed. This suggests that the tropospheric noise is correlated with topography. We also observe that the variation of tropospheric noise during the ascending data acquisition times is larger than during the descending data acquisition times. This is because the ascending data were acquired at local time 6:22 P.M. and the descending data were acquired at local time 6:20 A.M. The expected tropospheric phase signature is usually more significant around sunset than around sunrise. Note that the tropospheric noise variation is larger along the coast. This is because of the following reasons. First, the tropospheric noise along the coastal region is typically stronger. Second, the coastal region is farther away from the reference pixel location at GPS site MANE. As a result, tropospheric noise in the coastal region is less correlated with tropospheric noise at the reference location.

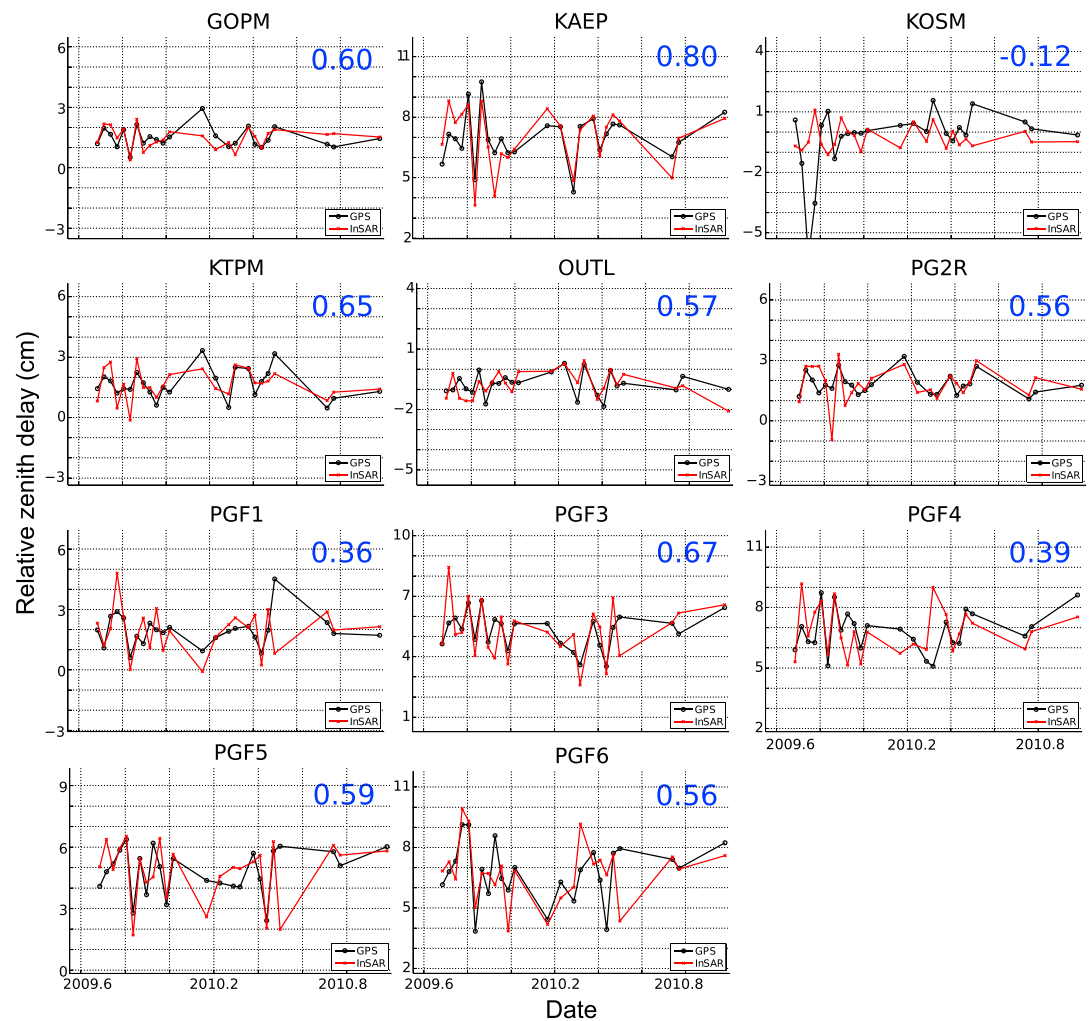


**Figure 16.** Relative tropospheric zenith delays as estimated from ascending InSAR data (in red) and GPS data (in black) at 11 Kilauea GPS stations. Here we select the GPS station MANE as the reference station for processing both InSAR and GPS data. The correlation coefficients between the InSAR and GPS-driven tropospheric delay time series are given in blue for each panel.

## 6. Conclusion

We developed an SBAS algorithm to extract both transient and secular ground deformations on the order of millimeters in the presence of tropospheric noise on the order of centimeters, when the transient is of short duration and known time and the background deformation is linear in time. We applied this algorithm to study the 2010 slow slip event as well as the secular motion at Kilauea. The east and vertical ground deformation time series we reconstructed are consistent with GPS time series over the same period. We observe that the coastal region on the south side of the Hilina Pali moves at a higher rate than the region north side of the Pali. We also conclude that the 2010 SSE displacement is mainly horizontal and the maximum magnitude of the 2010 SSE vertical component is less than 5 mm.

The algorithm proposed in section 3 can be modified to isolate a transient jump superimposed on any continuous background motion, including, but not limited to, constant velocity background motion. While this algorithm solves for ground deformation time series with high accuracy and fine spatial resolution, there are also some limitations. First, we cannot determine if any displacements during the SSE were concentrated at the Hilina and Holei Palis because of the spatial smoothness constraint we employ on the jump estimate. Second, InSAR only measures relative motions between pixels. To calibrate the missing constant in the InSAR ground deformation solution, it is necessary to know the magnitude of the ground deformation

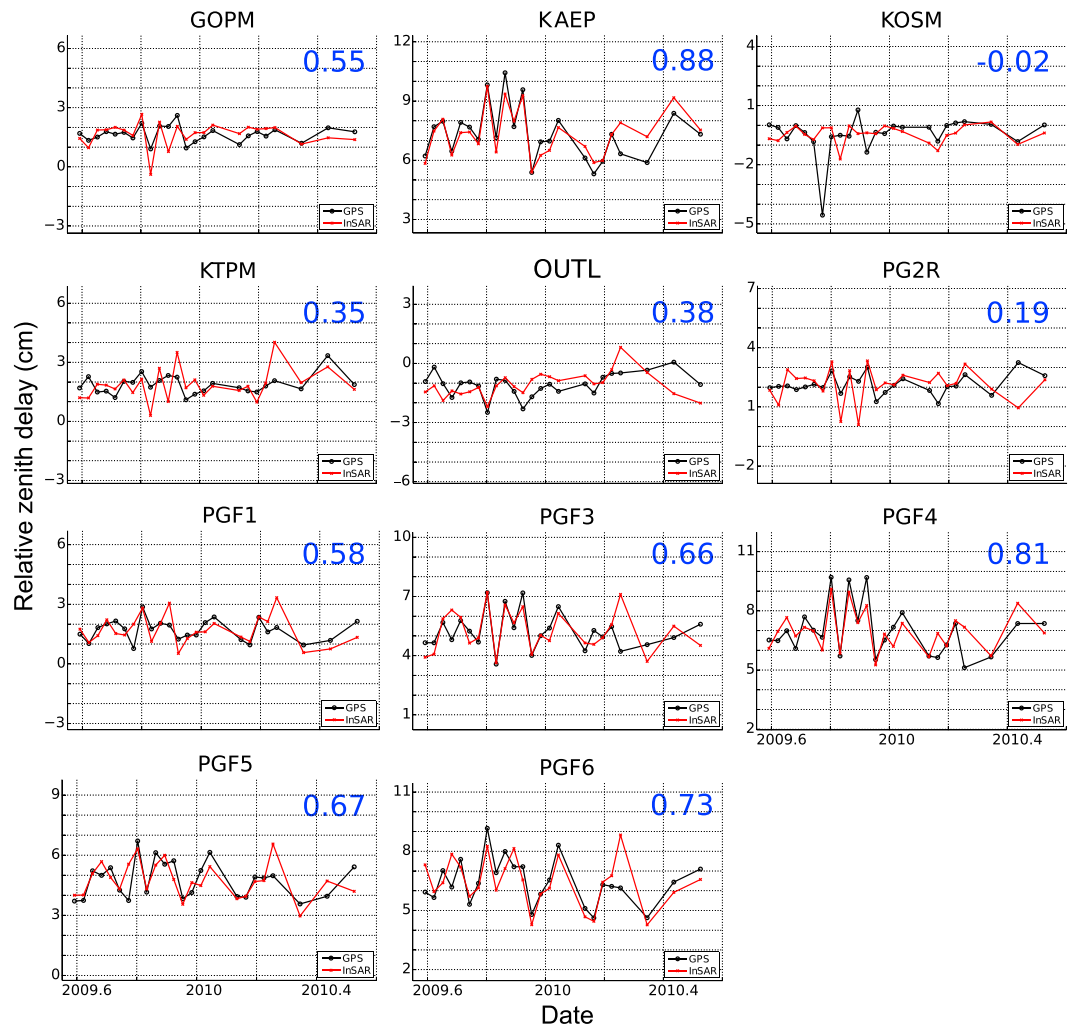


**Figure 17.** Relative tropospheric zenith delays as estimated from descending InSAR data (in red) and GPS data (in black) at 11 Kilauea GPS stations. Here we select the GPS station MANE as the reference station for processing both InSAR and GPS data. The correlation coefficients between the InSAR and GPS-driven tropospheric delay time series are given in blue for each panel.

(east, north, and up) at a reference pixel location as prior information. Third, the magnitude of the transient displacement at another pixel location is also needed to determine the optimal weighting for the spatial smoothness constraint. We choose GPS data from two GPS stations, KAEP and MANE, as our reference in this study. If GPS data are not available, other ground deformation measurements can be used as prior information. Note that only ground deformation magnitude at two pixel locations is needed to reconstruct the 2-D InSAR ground deformation map. Last, we cannot infer the north component of the ground deformation using only ascending and descending SAR data. Multiaperture interferometry (MAI) [Bechor and Zebker, 2006] techniques extract the along-track component of the ground deformation. In future studies, we may investigate using MAI to extract the north component of the ground deformation, as InSAR satellites usually operate in polar orbits.

We also estimate the tropospheric delay variation relative to a given reference pixel using the InSAR SBAS method. We verified that the InSAR relative tropospheric zenith delay estimates are strongly correlated with independent GPS tropospheric zenith delay estimates for the same time period. We conclude that it is possible to use InSAR data to reconstruct high-resolution tropospheric noise maps at each SAR acquisition time, which helps to visualize the tropospheric noise distribution in InSAR data. In case that a SAR data set is highly corrupted by tropospheric noise, we can discard this data set or assign it a smaller weight.

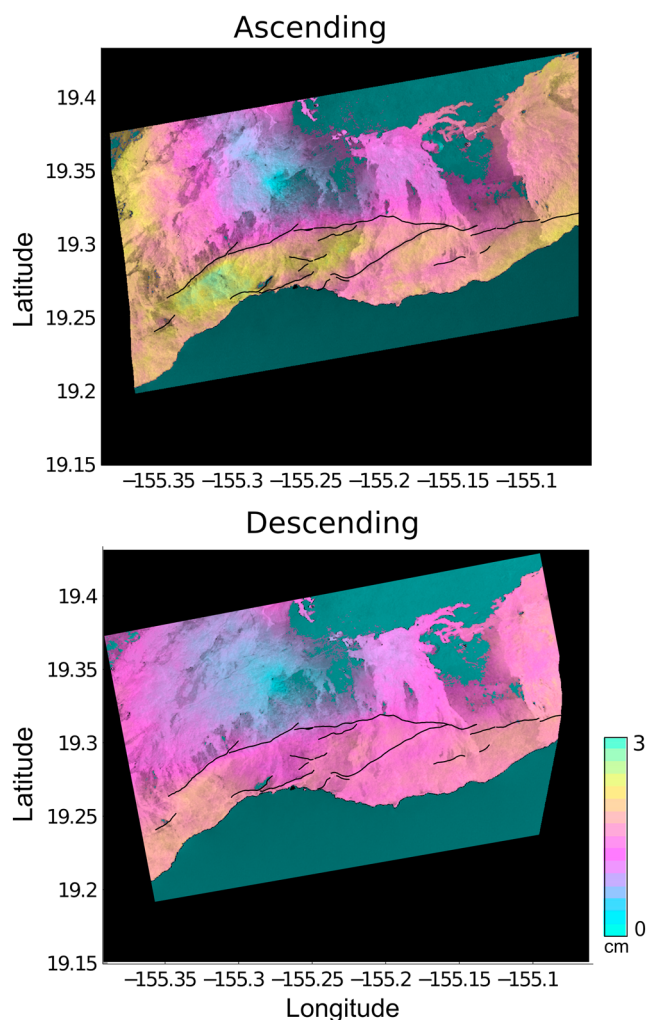


**Figure 18.** Standard deviation of the relative tropospheric noise time series at each pixel as derived from ascending and descending TerraSAR-X interferograms. The major faults of the Hilina Fault System are marked with black lines.

#### Acknowledgments

This work is partially funded by the NASA Earth Science and Interior program. The authors would like to thank the TerraSAR-X team of German Aerospace Center (DLR) for providing TerraSAR-X SSC data. The authors would like to thank the Hawaii Super-site for providing InSAR data over Hawaii. The authors would like to thank M.P. Poland from the U.S. Geological Survey for his discussions and suggestions that significantly improved this paper.

#### References

- Bechor, N. B. D., and H. A. Zebker (2006), Measuring two-dimensional movements using a single InSAR pair, *Geophys. Res. Lett.*, *33*(16), L16311, doi:10.1029/2006GL026883.
- Berardino, P., G. Fornaro, R. Lanari, and E. Sansosti (2002), A new algorithm for surface deformation monitoring based on small baseline differential SAR interferograms, *IEEE Trans. Geosci. Remote Sens.*, *40*(11), 2375–2383, doi:10.1109/TGRS.2002.803792.
- Brooks, B. A., J. H. Foster, M. Bevis, L. N. Frazer, C. J. Wolfe, and M. Behn (2006), Periodic slow earthquakes on the flank of Kilauea Volcano, Hawaii, *Earth Planet. Sci. Lett.*, *246*(3–4), 207–216, doi:10.1016/j.epsl.2006.03.035.
- Brooks, B. A., J. Foster, D. Sandwell, C. J. Wolfe, P. Okubo, M. Poland, and D. Myer (2008), Magmatically triggered slow slip at Kilauea Volcano, Hawaii, *Science*, *321*, 1177, doi:10.1126/science.1159007.
- Cervelli, P., P. Segall, K. Johnson, M. Lisowski, and A. Miklius (2002), Sudden aseismic fault slip on the south flank of Kilauea Volcano, *Nature*, *415*, 1014–1018.
- Chen, C. W., and H. A. Zebker (2002), Phase unwrapping for large SAR interferograms: Statistical segmentation and generalized network models, *IEEE Trans. Geosci. Remote Sens.*, *40*, 1709–1719.
- Chen, J., and H. A. Zebker (2012), Ionospheric artifacts in simultaneous L-band InSAR and GPS observations, *IEEE Trans. Geosci. Remote Sens.*, *50*, 1227–1239, doi:10.1109/TGRS.2011.2164805.
- Dragert, H., K. Wang, and G. Rogers (2004), Geodetic and seismic signatures of episodic tremor and slip in the northern Cascadia subduction zone, *Earth Planets Space*, *56*, 1143–1150.
- Fialko, Y., D. Sandwell, D. Agnew, M. Simons, P. Shearer, and B. Minster (2002), Deformation on nearby faults induced by the 1999 Hector Mine earthquake, *Science*, *297*, 1858–1862, doi:10.1126/science.1074671.
- Foster, J., B. Brooks, T. Cherubini, C. Shacat, S. Businger, and C. L. Werner (2006), Mitigating atmospheric noise for InSAR using a high resolution weather model, *Geophys. Res. Lett.*, *33*, L16304, doi:10.1029/2006GL026781.
- Hanssen, R. (2001), *Radar Interferometry: Data Interpretation and Error Analysis*, Remote Sensing and Digital Image Processing, Springer.
- Hirose, H., K. Hirahara, F. Kimata, N. o. Fujii, and S. Miyazaki (1999), A slow thrust slip event following the two 1996 Hyuganada earthquakes beneath the Bungo Channel, southwest Japan, *Geophys. Res. Lett.*, *26*(21), 3237–3240, doi:10.1029/1999GL010999.

- Hooper, A. (2008), A multi-temporal InSAR method incorporating both persistent scatterer and small baseline approaches, *Geophys. Res. Lett.*, *35*, L16302, doi:10.1029/2008GL034654.
- Lanari, R., O. Mora, M. Manunta, J. Mallorqui, P. Berardino, and E. Sansosti (2004), A small-baseline approach for investigating deformations on full-resolution differential SAR interferograms, *IEEE Trans. Geosci. Remote Sens.*, *42*(7), 1377–1386, doi:10.1109/TGRS.2004.828196.
- Larson, K. M., A. R. Lowry, V. Kostoglodov, W. Hutton, O. Sánchez, K. Hudnut, and G. Suárez (2004), Crustal deformation measurements in Guerrero, Mexico, *J. Geophys. Res.*, *109*, B04409, doi:10.1029/2003JB002843.
- Lauknes, T. (2011), InSAR tropospheric stratification delays: Correction using a small baseline approach, *IEEE Geosci. Remote Sens. Lett.*, *8*(6), 1070–1074, doi:10.1109/LGRS.2011.2156381.
- Massonnet, D., M. Rossi, C. Carmona, F. Adragna, G. Peltzer, K. Feigl, and T. Rabaute (1993), The displacement field of the Landers earthquake mapped by radar interferometry, *Nature*, *364*, 138–142, doi:10.1038/364138a0.
- Misra, P., and P. Enge (2006), *Global Positioning System: Signals, Measurements, and Performance*, Ganga-Jamuna Press.
- Montgomery-Brown, E. K., P. Segall, and A. Miklius (2009), Kilauea slow slip events: Identification, source inversions, and relation to seismicity, *J. Geophys. Res.*, *114*, B00A03, doi:10.1029/2008JB006074.
- Montgomery-Brown, E. K., C. H. Thurber, C. J. Wolfe, and P. Okubo (2013), Slow slip and tremor search at Kilauea Volcano, Hawaii, *Geochem. Geophys. Geosyst.*, *14*, 367–384, doi:10.1002/ggge.20044.
- Moore, J. G., D. A. Clague, R. T. Holcomb, P. W. Lipman, W. R. Normark, and M. E. Torresan (1989), Prodigious submarine landslides on the Hawaiian Ridge, *J. Geophys. Res.*, *94*(B12), 17,465–17,484, doi:10.1029/JB094iB12p17465.
- Poland, M., et al. (2010), Slow slip event at Kilauea Volcano, *Eos Trans. AGU*, *91*(13), 118–119, doi:10.1029/2010EO130002.
- Rosen, P., S. Hensley, I. Joughin, F. K. Li, S. Madsen, E. Rodriguez, and R. M. Goldstein (2000), Synthetic aperture radar interferometry, *Proc. IEEE*, *88*(3), 333–382, doi:10.1109/5.838084.
- Schmidt, D. A., and R. Bürgmann (2003), Time-dependent land uplift and subsidence in the Santa Clara Valley, California, from a large interferometric synthetic aperture radar data set, *J. Geophys. Res.*, *108*(B9), 2416, doi:10.1029/2002JB002267.
- Segall, P., E. K. Desmarais, D. Shelly, A. Miklius, and P. Cervelli (2006), Earthquakes triggered by silent slip events on Kilauea Volcano, Hawai'i, *Nature*, *442*, 71–74, doi:10.1038/nature04938.
- Shirzaei, M., R. Bürgmann, J. Foster, T. Walter, and B. Brooks (2013), Aseismic deformation across the Hilina fault system, Hawaii, revealed by wavelet analysis of InSAR and GPS time series, *Earth Planet. Sci. Lett.*, *376*, 12–19, doi:10.1016/j.epsl.2013.06.011.
- Wolfe, C. J., B. A. Brooks, J. H. Foster, and P. G. Okubo (2007), Microearthquake streaks and seismicity triggered by slow earthquakes on the mobile south flank of Kilauea Volcano, Hawai'i, *Geophys. Res. Lett.*, *34*, L23306, doi:10.1029/2007GL031625.
- Zebker, H., and J. Villasenor (1992), Decorrelation in interferometric radar echoes, *IEEE Trans. Geosci. Remote Sens.*, *30*(5), 950–959, doi:10.1109/36.175330.